

# Realization of Ultrathin Waveguides by Elastic Metagratings

**Yabin Hu**

Northwestern Polytechnical University

**Yunhao Zhang**

Xi'an Jiaotong University

**Guangyuan Su**

Xi'an Jiaotong University

**Meiying Zhao**

Northwestern Polytechnical University

**Bing Li**

Northwestern Polytechnical University <https://orcid.org/0000-0002-6951-1373>

**Yongquan Liu** (✉ [liy2018@xjtu.edu.cn](mailto:liy2018@xjtu.edu.cn))

Xi'an Jiaotong University

**Zheng Li**

Peking University

---

## Article

**Keywords:** Realization, ultrathin waveguides, elastic metagratings, Guiding transports, waves

**Posted Date:** September 9th, 2021

**DOI:** <https://doi.org/10.21203/rs.3.rs-734570/v1>

**License:**  This work is licensed under a Creative Commons Attribution 4.0 International License.

[Read Full License](#)

---

**Version of Record:** A version of this preprint was published at Communications Physics on March 17th, 2022. See the published version at <https://doi.org/10.1038/s42005-022-00843-0>.

# Realization of ultrathin waveguides by elastic metagratings

Yabin Hu<sup>1</sup>, Yunhao Zhang<sup>2</sup>, Guangyuan Su<sup>2</sup>, Meiyang Zhao<sup>1</sup>, Bing Li<sup>1</sup>\*, Yongquan Liu<sup>2</sup>\*, Zheng Li<sup>3</sup>

<sup>1</sup> *School of Aeronautics, Northwestern Polytechnical University, Xi'an, Shaanxi, 710072, China*

<sup>2</sup> *State Key Laboratory for Strength and Vibration of Mechanical Structure, School of Aerospace Engineering, Xi'an Jiaotong University, Xi'an, 710049, China*

<sup>3</sup> *Department of Mechanics and Engineering Science, Peking University, Beijing 100871, China*

\*Corresponding author E-mail address: [bingli@nwpu.edu.cn](mailto:bingli@nwpu.edu.cn); [liuy2018@xjtu.edu.cn](mailto:liuy2018@xjtu.edu.cn)

## Abstract

Guiding transports of classical waves has inspired a wealth of nontrivial physics and momentous applications in a wide range of fields. To date, a robust and compact way to guide energy flux travelling along an arbitrary, prescheduled trajectory in a uniform medium is still a fundamental challenge. Here we propose and experimentally realize a generic framework of ultrathin waveguides for full-angle wave trapping and routing. The metagrating-based waveguide can totally suppress all high-order parasitic diffractions to efficiently route guided elastic waves without leakage. Remarkably, the proposed waveguide prototype works in a broad frequency range from 12 to 18 kHz and regardless of the incident angle. An analytical slab-waveguide model is further presented to predict and tailor the diffracted patterns in the metagrating-based waveguide. Compared with existing methods based on topological edge states or defected metamaterials, our meta-waveguide strategy exhibits absolute advantages in compact size, robust performance, and easy fabrication, which may provide a new design paradigm for vibration control in solids, wave steering in electromagnetics, acoustics and other waves.

## Introduction

Guiding waves in a desired manner plays an essential role in long-distance energy transport and thus remains as a hot topic in both fundamental physics and applied science<sup>1</sup>. The origin of waveguide can be traced back to the first “Light Fountain” experiment conducted by Jean-Daniel Colladon in 1842<sup>2,3</sup>. Due to the total-internal-reflection (TIR) beyond a critical incidence angle, the light was trapped inside the “water channel” with a higher refractive index than the surrounding air. This light-guiding fancy has inspired not only modern telecommunication and sensing devices like optical fibers<sup>3,4</sup>, but also the ongoing developments of guided-mode physics for slab-waveguides<sup>5</sup>, nonlinear optics<sup>6</sup> and optical cavities<sup>7</sup>. However, such a high-index waveguide paradigm is only available for partial incidence angles. In contrast, an omnidirectional total-wave-trapping in highly confined waveguide can be only realized by introducing extremely mismatched (soft/hard) impedance boundaries<sup>5,8</sup>. For example, in an airborne waveguide, air and solids serve as the waveguiding and extremely hard surrounding media, respectively. It seems unprocurable to realize a waveguide between arbitrary media with similar impedances or even in an uniform medium.

To this end, guiding waves along an arbitrary path has been enabled by artificially exotic media, such as acoustic/elastic metamaterials with well-engineered defects<sup>9-11</sup>. By underpinning band gaps and periodically arranged defects in sonic crystals or metamaterials, we can confine wave paths in the defected area and guide wave propagation along a prospective route, even regardless of sharp corners. Nevertheless, the inherent narrow working band, energy leakage and large footprints still pose insurmountable obstacles for the popularization of this method. As another emerging scheme, nontrivial topological phases have rapidly ushered in a significant

revival of waveguide fashion in very recent decade<sup>12-15</sup>. Achieved by the analogues of quantum/quantum-spin Hall effect<sup>14</sup>, Dirac cones<sup>13,16</sup>, gapless states<sup>17</sup> or Weyl systems<sup>18,19</sup>, topological edge states have realized robust acoustic/elastic waveguides, which are stable against local perturbations and capable of backscattering immune. However, apart from poor coupling with the background media, the topological waveguide framework still suffers from the challenges of extremely narrow bandwidth, rigorously exquisite complexity and bulky volume. Such severe constraints are so general in all existing designs that undeniably hinder the technical availability and fabrication feasibility to a large extent.

Alternatively, the recently proposed metasurface promises a thriving future for wavefront steering with a more compact footprint and thus an easy-fabricated low-dimension design<sup>20-26</sup>. Without losing functionality, metasurfaces are capable of great flexibility and rich wave phenomena, such as wave shaping<sup>25-28</sup>, absorbing<sup>29-31</sup> and isolating<sup>32,33</sup>. These versatile modulation abilities arise from the well-tailored abrupt phase variation, which can be programmed by the generalized Snell's law (GSL)<sup>20</sup>,  $(\sin\theta_o - \sin\theta_i)k_0 = n\xi$ , where  $\theta_i$  and  $\theta_o$  are the angles of incident and outgoing waves,  $\xi = d\phi/dx$  is the phase gradient and the integer  $n$  denotes the diffraction mode. Based on the GSL, it is easy to see that the  $0^{th}$  transmitted mode ( $n = 0$ ) is always existing, which indicates that the waves can transmit unavoidably from one side to another side. As a result, an efficient total-wave-blocking seems impossible, let alone a further waveguiding using metasurfaces. Excitingly, metagrating was very recently demonstrated promising in remedying this capability limitation of metasurface<sup>34-36</sup>. Emphasizing on the unity efficiency, metagratings can modify the GSL with a supercell concept, which consists of only a few (or even single) unit cells. By doing this, anomalous refractions or/and reflections of every

higher-order diffraction mode could be coherently assigned<sup>36,37</sup>. It is noteworthy, as an essential factor, each sub-unit in the metagrating should be high-efficient to guarantee the whole steering efficiency. However, more to the point of total-wave-trapping, the existing local-resonance-based designs are not sufficient to satisfy such criteria<sup>33,38</sup>. To the best of our knowledge, no work has been reported on a high-efficient, broadband, omnidirectional wave-blocking by metagratings or metasurfaces. Thus far, a physical realization of compact waveguide for all-directional wave-trapping and guiding remains an outstanding fundamental challenge.

In this work, by employing a bipartite metagrating paradigm, we propose an ultrathin waveguide framework for omnidirectional trapping and efficient routing of elastic-waves under a full-angle source excitation. Only using two unit-cells as a subwavelength supercell, we present theoretically and experimentally that the ultrathin waveguide can isolate all wave orders and guide elastic-waves along an arbitrary path. Moreover, an analytical slab-waveguide model is proposed to predict and steer the guided-mode physics. Fundamentally distinct from the topological edge states or defected metamaterials, we demonstrate that the proposed waveguide system exhibits a nontrivially ultrathin, robust and broadband guiding feature.

## Results

**Design paradigm and mechanism.** Figure 1a illustrates the schematic of an ultrathin waveguide routing along an arbitrary path for flexural waves in a plate. It consists of two layers of thin elastic metagratings to function as curbs of the propagation path. To achieve efficient wave routing without leakage, the unique property of our metagratings is that they can totally reflect incident waves from any directions, as illustrated in Fig. 1b. To this end, we design the metagratings based on the following mechanism. We first introduce a passive elastic metagrating with periodically

repeated supercells. Each supercell, composed of only two unit-cells ( $m = 2$ ) and with a period length  $L$ , leads to a phase gradient  $\xi = 2\pi/L$ . Based on the modified GSL of metagratings proposed by Fu et al<sup>36</sup> in 2019,

$$\begin{cases} \sin\theta_i + n\frac{\lambda}{L} = \sin\theta_t, & m + n = \text{odd} \\ \sin\theta_i + n\frac{\lambda}{L} = \sin\theta_r, & m + n = \text{even} \end{cases} \quad (1)$$

where  $\lambda$  is the wavelength,  $n$  is the diffraction order, subscripts  $t$  and  $r$  represent the transmitted and reflected waves, respectively. It indicates that the selection of transmission or reflection performance for the outgoing waves can be determined by the integer-parity design of metagratings, which has been experimentally verified recently in both acoustics<sup>36</sup> and elastodynamics<sup>37</sup>. Based on Eq. (1), we then introduce the following design criteria to the elastic metagrating,

$$\frac{\lambda}{L} > 2 \quad (2)$$

By doing this, only  $n = 0$  is permitted under such design, all the other diffraction orders can be totally suppressed. Recalling that  $m = 2$  is selected as an even number here, it is evident that an efficient specular reflection with  $\theta_r = \theta_i$  can be achieved regardless of the incident angle. In this way, by assembling two omnidirectionally reflected metagratings along an arbitrary route, we can totally trap and guide waves at will.

The omnidirectionally specular reflection of our metagratings can also be interpreted from a diffraction-based perspective in the  $k$ -space. As illustrated in Fig. 1c, upon the incident wave, the metagrating with period  $L$  and wave number  $\xi = 2\pi/L$  generates multiple diffraction modes, which are depicted by the green arrows. Due to the integer-parity design of metagratings ( $m = 2$  here), the directions of arrows are different for different modes based on Eq. (1). It is important to note that, although infinite modes can be excited according to the diffraction theory, most modes

are evanescent within the near field. As a result, only a few diffraction modes in the range of  $k_x \in [-k_0, k_0]$  can be propagated into the far field, where  $k_0 = 2\pi/\lambda$  is the wave number of the background medium. It is readily to see that, in the case of  $\xi > 2k_0$  (corresponding to  $\lambda/L > 2$ ), there exists only one propagating mode, i.e., the  $0^{th}$  order mode referring to specular reflection.

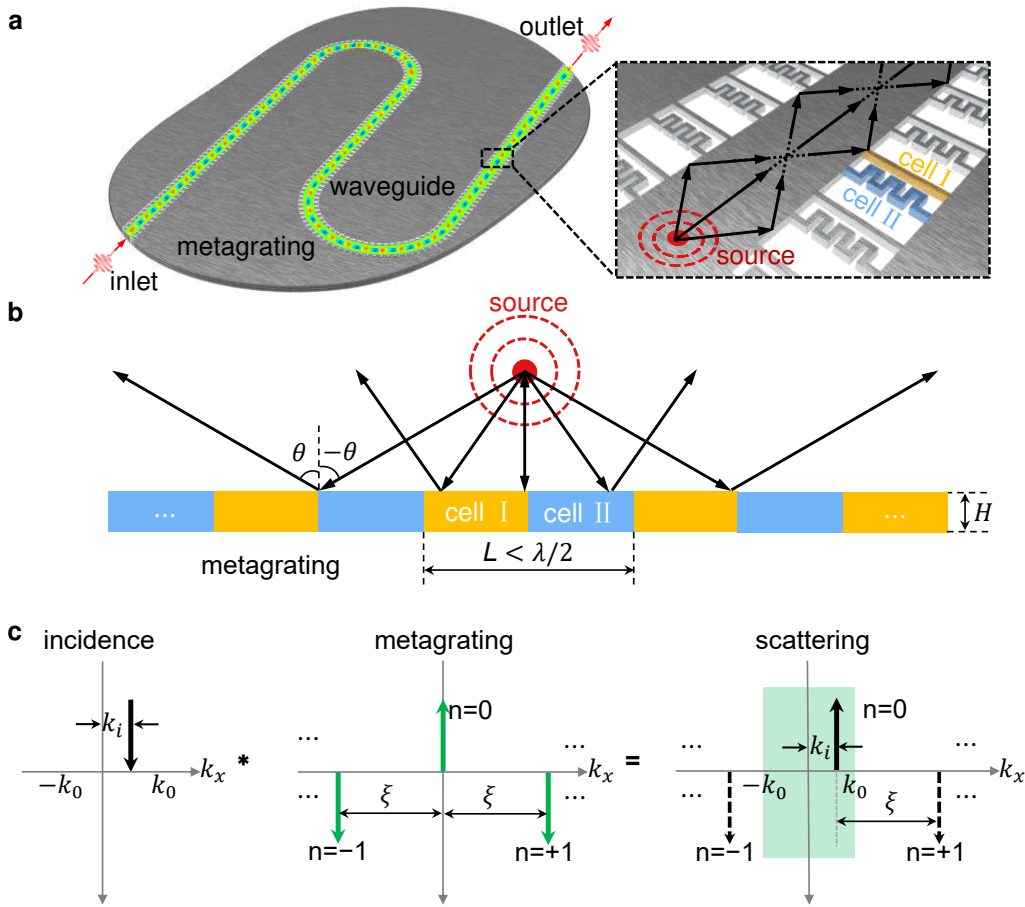


**Figure 1 | Metagrating-based ultrathin waveguide.** (a) Schematic of the proposed waveguide constructed by two layers of elastic metagratings to confine the waves along an arbitrary route. The supercell, consisting of only two unit-cells, is periodically distributed in each metagrating. (b) The metagrating can omnidirectionally block flexural waves in a thin plate in the form of specular reflection. The interval of periodically repeated supercells  $L$  is less than half of the wavelength. (c) A diagram for how the metagrating omnidirectionally reflect an incident wave.  $k_x$  denotes the wavenumber along the metagrating. Upward (downward) arrows represent the reflection (transmission) of waves. The green box is the regime of propagation modes.

At the end of this part, we would like to stress that the proposed waveguide is composed of two thin layers only, which exhibits great advantages in compact size than previous strategies of

defected phononic crystals or topological metamaterials. It should also be mentioned that, although this metagrating-based waveguide focuses on flexural waves in plates here, it is also applicable to other types of waves, such as the waves in plasma, electromagnetism and acoustics.

**Realization of the omnidirectionally reflected metagrating.** As depicted in the inset of Fig. 1a, for each supercell, we propose a straight beam and a zigzag-type one as unit cells I and II, respectively. The phase shift between the two unit-cells is set as  $\pi$ , i.e.,  $\Delta\phi = \pi$ , to realize a phase wrap of  $2\pi$  per supercell. Unit cells are built by digging holes in thin steel plates with thickness  $D = 1.5$  mm throughout the study. The length of the supercell  $L = 14$  mm is designed as  $0.46\lambda$  at 15 kHz ( $\lambda = 30.6$  mm), and the metasurface width  $H$  is  $0.67\lambda$ . Fig. 2a illustrates the transmittance  $|t|$  as a function of  $\theta_i$  at the operating frequency of 15 kHz for each individual unit cell and the supercell after combination. Due to the set-up limitation, the range of the incident angle  $\theta_i \in [-80^\circ, 80^\circ]$  is exhibited. See the [Supplementary Fig. 1](#) and [Supplementary Note 1](#) for more details. A nearly total transmission ( $|t| \cong 1$ ) is always observed for both individual cell I and cell II. On the contrary, a low transmittance ( $|t| < 0.25$ ) is performed for the supercell with an alternate arrangement of the two unit-cells, regardless of the incident angle  $\theta_i$ . Such astonishing reversal of transmission under a full range of incident angles clearly demonstrates the feasibility of our design strategy of omnidirectionally reflected metagrating.

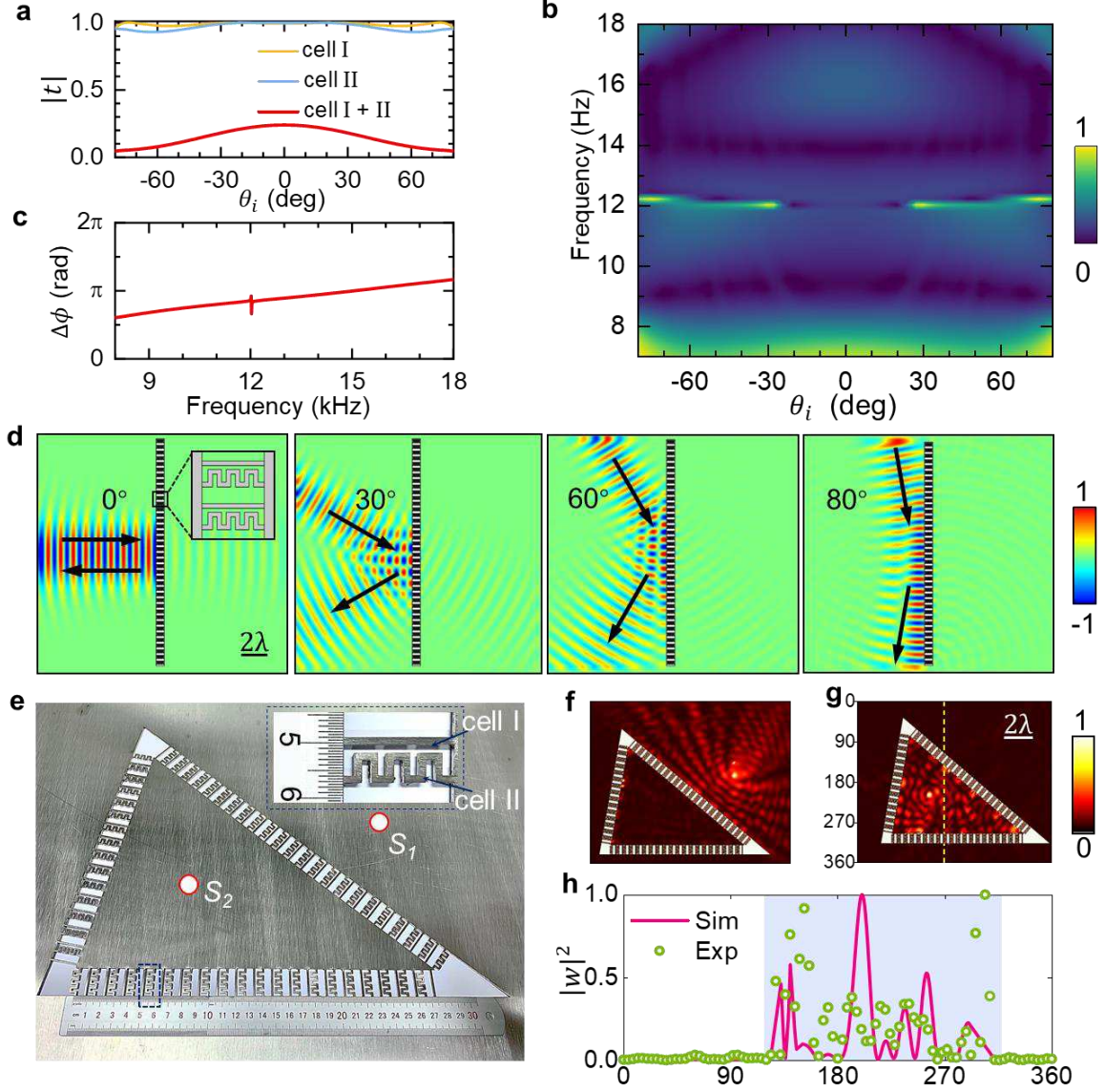


**Figure 2 | Omnidirectional reflection of the metagrating.** (a) Transmittance  $|t|$  at 15 kHz as a function of the incident angle  $\theta_i$ . (b)  $|t|$  as functions of  $\theta_i$  and the operating frequency  $f$ . (c) The phase difference  $\Delta\phi = \phi_I - \phi_{II}$  of the two unit cells as a function of  $f$ . (d) Nearly total reflections are numerically observed for incident angles of  $0^\circ, 30^\circ, 60^\circ$  and  $80^\circ$ , respectively. Theoretical loci are plotted as black arrows. (e) Sample of a triangle-shaped omnidirectional isolator enclosed by the proposed metagratings. (f) Experimentally measured energy field when a point source  $S_1$  is placed outside the enclosed region. (g) The measured energy field when a point source  $S_2$  is located inside the enclosed region. (h) Experimental and simulated distributions of normalized energy (equivalent to the square of the displacement amplitude  $|w|^2$ ) along the dashed yellow line in g.

To evaluate the robustness of the proposed metagrating, we further investigate the transmittance  $|t|$  at different frequencies  $f$  and  $\theta_i$  in Fig. 2b. Remarkably,  $|t|$  maintains a stably small value (less than 0.32, corresponding to 10% of energy) for all incident angles within

a wide operating frequency range of 8~18 kHz, except for an abrupt disturbance near 12 kHz. The broadband robustness of the omnidirectional reflection stems from the relatively stable phase shift between the two unit cells, as illustrated in Fig. 2c. It is noted that  $\Delta\phi$  maintains an approximate value to  $\pi$  in the frequency range of 8~18 kHz, although the supercell is designed exactly for 15 kHz. The slight variation roughly satisfies the design criterion of  $2\pi$ -phase-wrap per supercell, leading to a broadband performance of omnidirectional reflection. Furthermore, it is evident that there is an abrupt peak at 12 kHz, which corresponds to an ultra-narrow disturbance in the transmittance contour. This point is induced by the twisting resonance of unit cell II (see further discussions in [Supplementary Fig. 2](#) and [Supplementary Note 2](#)).

Full-wave simulations of the displacement fields for flexural waves ( $A_0$ -mode) at 15 kHz in a thin steel plate are visualized in Fig. 2d. Different oblique incidences ( $\theta_i = 0^\circ, 30^\circ, 60^\circ, 80^\circ$ ) are performed as examples, respectively. Obviously, a nearly total reflection is achieved regardless of the incident angle, which agrees well with the results in Fig. 2a. At all incident angles, the specular reflection is observed, which indicates that only the diffraction mode  $n = 0$  is generated by the proposed metagrating. In all cases, the numerical field spectrums show perfect agreement with theoretical predictions based on Eq. (1).

The omnidirectional reflection of the metagrating is further proposed to trap the waves and vibrations. As illustrated in Fig. 2e, the metagrating can be arranged to construct an enclosed region with an arbitrary shape, for example a triangular area. The cases of other exotic shapes are also performed in the [Supplementary Fig. 4](#) and [Supplementary Note 4](#). The metagrating is fabricated by wire electrical-discharge machining in a steel plate with thickness 1.5 mm. Two point sources  $S_1$  and  $S_2$ , excited by piezoelectric wafers, are confined outside and inside the

enclosed region, respectively. A laser Doppler vibrometer (Polytec, NLV-2500) is used to capture and visualize the full wave field of  $A_0$ -mode Lamb wave. Detailed experimental setups are described in [Supplementary Fig. 6](#). If the point source  $S_1$  (or  $S_2$ ) is placed outside (or inside) the enclosed region in Fig. 2f (or Fig. 2g), almost all waves are bounced back by the metagrating boundary (or confined in the triangle region). Therefore, the metagrating acts like a “cage” to almost totally trap the wave energy and isolate it from outside. Significantly, this isolation performance is omnidirectional, and no wave leakage occurs in a full-angle range. We further quantitatively evaluate the normalized energy along a straight line across the “cage” boundary (the yellow dashed line in Fig. 2g). As shown in Fig. 2h, the square of the displacement amplitude  $|w|^2$  has a striking drop from oscillated high values inside the metagrating ( $122 \text{ mm} < x < 309 \text{ mm}$ , shaded in blue) to less than 0.01 outside. The experimentally measured results (marked as green dots) are well consistent with the simulated profile (marked as the magenta curve). Moreover, we would like to stress that the cage effect is quite robust to the frequency and works once the wave touches the metagrating. To unambiguously illustrate this point, the corresponding transient responses of the whole wave propagation are numerically and experimentally captured (see [Supplementary Movies 1-4](#)). The omnidirectional cage effect at other frequencies (13~15 kHz) are also performed in the [Supplementary Fig. 3](#) and [Supplementary Note 3](#).

**Arbitrary waveguide routing.** We further construct a series of ultrathin waveguides with arbitrary routing paths by utilizing the omnidirectionally reflected metagratings as curbs of the waveguides. As shown in Fig. 3a, a  $L$ -shape waveguide with channel width  $l = 45 \text{ mm}$  is firstly fabricated by parallel alignment of two designed metagratings. The turning part of the waveguide sample is enlarged as the inset. Placing a piezoelectric wafer at the inlet point  $S$  as a full-angle

point source, one can see that almost all waves are restricted and trapped in the waveguide to propagate along the pre-designed channel with little leakage (Fig. 3b). It means that the metagrating-based waveguide is capable of guiding waves via omnidirectional reflection, like an optical slab-waveguide. The robust waveguiding feature is verified by the excellent agreements between the numerical and experimental energy fields at several adjacent frequencies from 13 to 15 kHz. In a more vivid way, the numerically and experimentally captured transient responses of the whole waveguiding process are provided in [Supplementary Movies 5 and 6](#).

We then conduct a quantitative analysis of the waveguiding efficiency by calculating the averaged displacement amplitude  $|w|_{ave} = \frac{1}{k} \sum_{j=1}^k |w|_j$  in three selected square regions (A, B, and C in Fig. 3a). Region A is placed inside the waveguide before the turning corner with a distance  $r_A=95$  mm to the point source  $S$ , while region B is in the vertical channel after the turning corner with a straight-line distance  $r_B=241$  mm to  $S$ . Region C is placed adjacent to B but just beyond the waveguide boundary, with  $r_C=188.3$  mm away from  $S$ . Taking region C as the reference region, we can define a contrast ratio  $\eta$  as  $\eta_{A/C} = 20lg(|w|_{ave}^A/|w|_{ave}^C)$  for region A, and  $\eta_{B/C} = 20lg(|w|_{ave}^B/|w|_{ave}^C)$  for region B. Without waveguide (w/o), this contrast ratio should be fixed values of  $\eta_{A/C} = 20lg\sqrt{r_C/r_A} = 3$  and  $\eta_{B/C} = 20lg\sqrt{r_C/r_B} = -1.1$  according to the diffusion attenuation theory (dashed lines in Fig. 3c), respectively. A higher value of  $\eta$  than the cases without waveguides indicates a better performance of the waveguide. The profiles of tested  $\eta$  as a function of frequency  $f$  are presented in Fig. 3c. Remarkably, in the thin plate with waveguide (w/), the value  $\eta_{A/C}$  keeps a stable high value of over 9.2 in the frequency range of 12~18 kHz and reaches a peak of around 17.8 at 17.2 kHz, implying a robust broadband feature. Thus, the contrast ratio has a striking enhancement by virtue of the

metagrating-based waveguide. Furthermore, the tested value  $\eta_{B/C}$  is always over the value without the waveguide in the frequency range 12~18 kHz. Specifically, in most of the frequency range (12~14.4 kHz and 16.4~17.4 kHz),  $\eta_{B/C}$  keeps over 8.0, although the region B is further away from the source than C. The significant enhancements in the contrast ratios clearly manifest the efficient routing and guiding performance of our waveguide strategy over a long travel distance and in a wide frequency range.

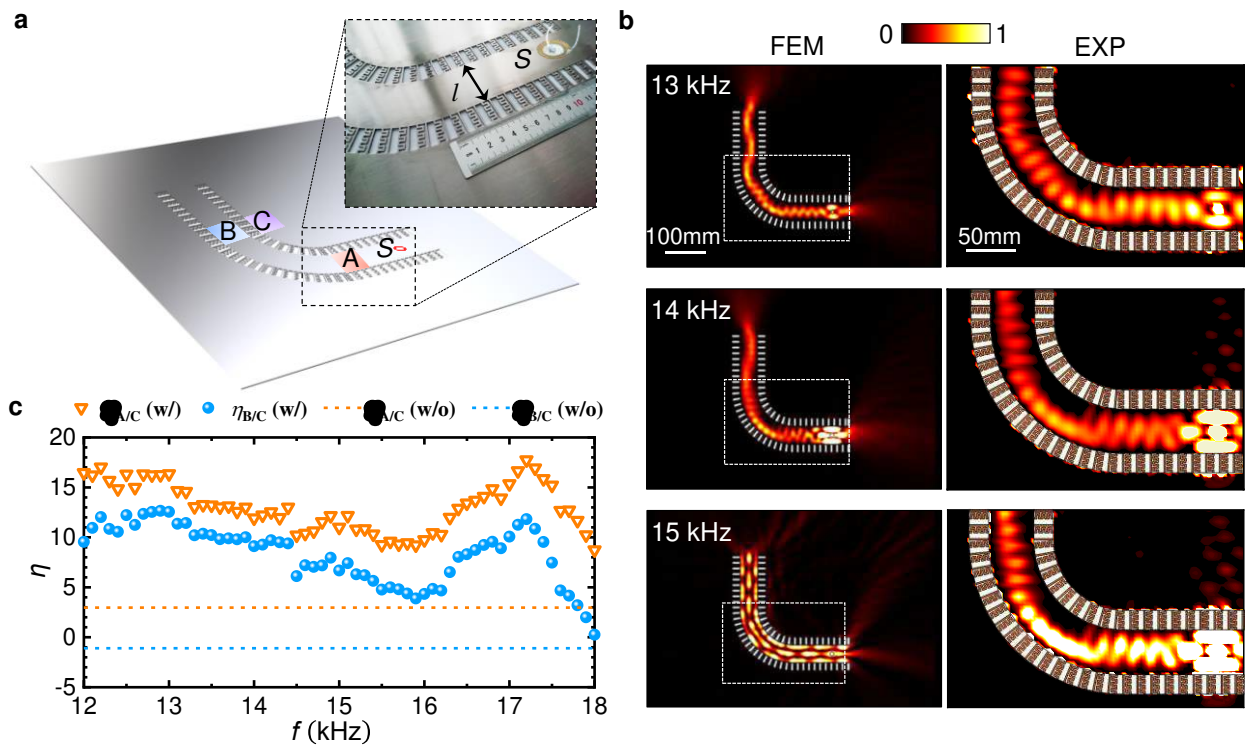


**Figure 3 | Experimental verification of efficient waveguide.** (a) Sample of an ultrathin L-shape waveguide made of metagratings. A piezoelectric wafer is bonded at point *S* to generate omnidirectional flexural waves. (b) Experimentally measured (EXP) and simulated (FEM) energy fields of the waveguide at 13~15 kHz. The tested region is framed by the white dashed box. (c) Contrast ratios  $\eta_{A/C}$  and  $\eta_{B/C}$  as a function of frequency  $f$ . Dots refer to the measured contrast ratio with (w/) the waveguide. Dashed curves refer to the theoretical contrast ratio without (w/o) waveguide.

A series of waveguides of various shapes are further designed to evaluate the robustness of the proposed strategy, as depicted in Fig. 4. It is verified that the waveguide could maintain a

highly efficient transmission even after continuous sharp corners, like a *N*-shape path (Fig. 4a). It could also route the omnidirectional waves to make a smooth U-turn with almost no leakage (Fig. 4b). Moreover, the waveguide framework could realize multiple elastic-wave propagation paths. As illustrated in Fig. 4c, two incident waves from point sources  $S_1$  and  $S_2$  can travel along two parallel paths without any influence with each other even the adjacent distance is less than one waveguide width. Furthermore, as shown in Fig. 4d, we can divide one elastic wave beam into two branches by using the waveguide junction for more functional switching routes. Such robust routing performance allows us to demonstrate a novel and highly efficient waveguide strategy with outstanding ultrathin footprint, which is totally distinct from topological states or defected metamaterials.

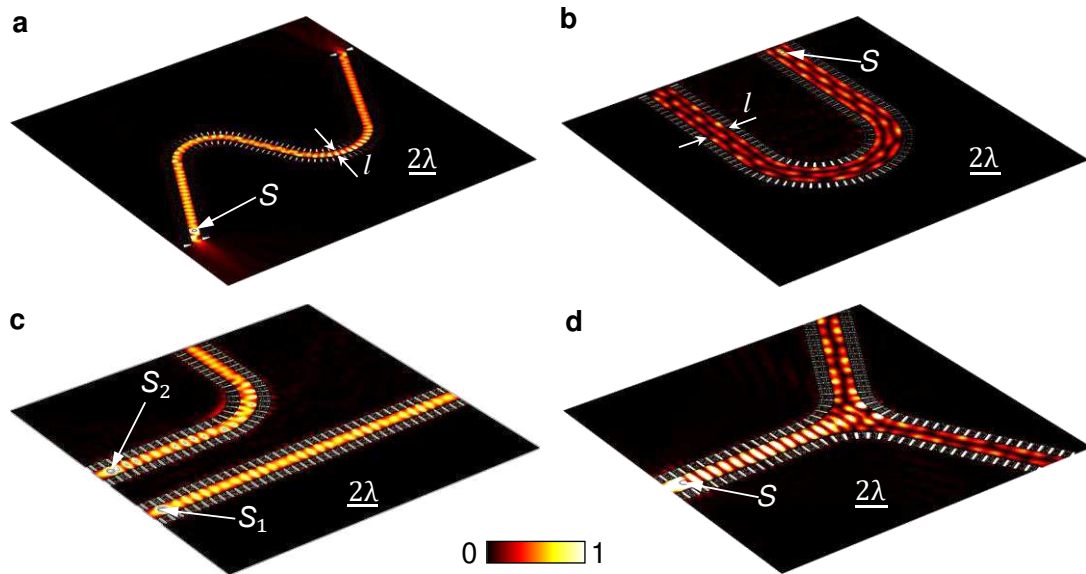


**Figure 4 | The proposed waveguide strategy for arbitrary routes at 15 kHz.** (a) Simulated energy fields of a “*N*”- shape waveguide with width  $l=0.82\lambda$ . (b) “*U*”- shape waveguide with width  $l=1.47\lambda$ . (c) Two adjacent waveguide paths with a distance of  $2\lambda$  ( $l=0.82\lambda$ ). (d) Wave splitting by a waveguide junction ( $l=\lambda$ ).

**Guided-mode theory in metagrating-based ultrathin waveguides.** It is observed in Fig. 4 that the guided wave fields through the metagrating-based waveguides have strong dependency on the

channel width  $l$ . Specifically, single or multiple rows of discrete standing wave packets are generated in waveguides with different normalized widths  $l/\lambda$ . We here show that such interesting field spectrums can be interpreted by the guided-mode theory. In consideration of the distinct difference from classical slab waveguides<sup>5</sup>, we propose a modified guided-mode theory to predict the guided-mode pattern in the metagrating-based waveguide for a full-angle wave incidence.

As illustrated in Fig. 5a, we first consider a pair of wave beams generated from the point source  $S$  and then propagating in the waveguide with incident angles  $\pm\theta_i$ , respectively. Different from classical waveguides using high-index heterogeneous materials<sup>5</sup>, the wave number  $k$  in the proposed waveguide is equal to that in the host plate. As discussed in previous sections, the wave beam is totally reflected at the metagrating and then travels in a zig-zag path. Once touching the metagrating, the wave beam will be mirrored back to the waveguide but with a phase shift  $\varphi$ . To have a guided mode, point  $A$  before boundary reflection and point  $C$  after boundary reflection possess the same phase with their projections  $B$  and  $D$ , respectively. Namely, the round-trip phase acquired by the ray must be an integer multiple of  $2\pi$ ,

$$k(AC - BD) - 2\varphi = 2\beta\pi \quad (3)$$

where  $\beta$  is an integer corresponding to the order of the guided mode  $N = \beta + 1$ . Noting that  $AC - BD = 2l \cos \theta_i$ , we have

$$\frac{l}{\lambda} = \frac{\beta\pi + \varphi}{2\pi \cos \theta_i} \quad (4)$$

As a special case, if we place the point source  $S$  in the middle of the waveguide, points  $A$  and  $E$  also have the same phase due to symmetry. Thus, the phase shift from  $E$  to  $B$  should also be an integer multiple of  $2\pi$ ,

$$kBE + \varphi = 2\gamma\pi \quad (5)$$

where  $\gamma$  is an integer. Compared Eq. (3) with Eq. (5), we have  $\beta = 2\gamma$  (or  $N = 2\gamma + 1$ ) with  $\gamma = 0, 1, 2, \dots$ , which means that only odd modes can be generated in the case of symmetric point source. Considering that  $\theta_i \in [-\frac{\pi}{2}, \frac{\pi}{2}]$ , Eq. (4) becomes  $\frac{l}{\lambda} = \frac{2\gamma\pi + \varphi}{2\pi c \cos\theta_i} \geq \gamma + \frac{\varphi}{2\pi}$ . It infers that when  $l/\lambda$  is less than a certain value  $\frac{\varphi}{2\pi}$ , the guided mode will disappear. This phenomenon is numerically verified in [Supplementary Fig. 5](#), where we find that waves are prohibited from travelling along the waveguide when  $l/\lambda$  is less than 0.2 (i.e.,  $\varphi = 0.4\pi$ ).

Figure 5b shows the variation of  $\gamma$  versus the ratio  $l/\lambda$  and the incident angle  $\theta_i$  based on the guided mode theory when the point source  $S$  is placed at the center of the waveguide. A general case of arbitrarily placed  $S$  is also supplied in [Supplementary Fig. 5](#) and [Supplementary Note 5](#). As illustrated, the guided-mode pattern can be manipulated by the waveguide width and the excitation frequency. For the value  $l/\lambda \in (0.2, 1.2]$ , only the branch  $\gamma = 0$  can be found in Eq. (4), inferring that only the guided-mode order  $N = 1$  exists. When the ratio is set as  $l/\lambda \in (1.2, 2.2]$ , we have  $\gamma = 0$  and  $\gamma = 1$  under the full-angle incidence. In this case, the guided-mode order is dominantly determined by the higher order  $N = 3$ . Similarly, we can predict  $N = 5$  for  $l/\lambda \in (2.2, 3.2]$ . As verifications, we checked the field patterns of three cases  $l/\lambda = 0.5, 1.5, 2.5$  in Fig. 5c, respectively. As expected, the guided-mode patterns are concordant with our analytical predictions. It is clearly presented that there are one, three, and five rows of standing wave beams within the waveguide accordingly. A yellow dashed line across the waveguide is further selected to quantify the wave-packets. Except the two distinct crests induced by the metagrating boundaries, the wave-packet number is exactly  $N = 1$ ,  $N = 3$  and  $N = 5$  in corresponding waveguides, respectively.

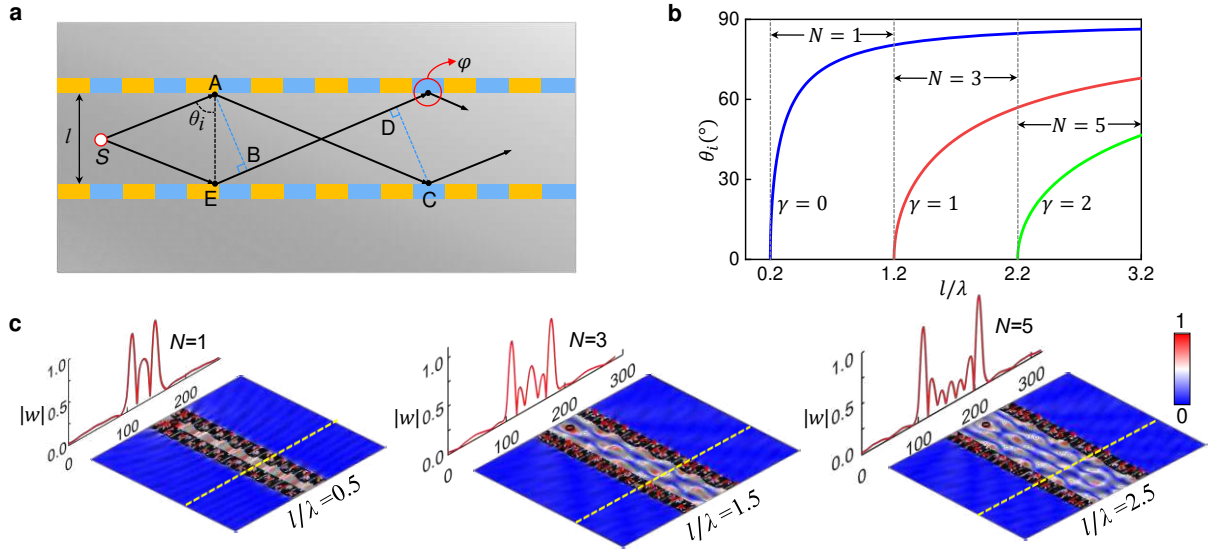


**Figure 5 | Guided-mode theory for waveguides.** (a) Schematic of omnidirectional wave reflection in a waveguide excited by a point source  $S$  placed in the middle of the waveguide. (b) The variation  $\beta$  as functions of the ratio  $l/\lambda$  and the incident angle  $\theta_i$ . The whole region is divided into three parts ( $N = 1$ ,  $N = 3$  and  $N = 5$ ), which represent different guided-mode orders. (c) Simulated displacement fields  $|w|$  in the waveguides with  $l/\lambda = 0.5, 1.5, 2.5$ , respectively. The amplitude  $|w|$  on a typical line (dashed yellow line) crossing the waveguide (the orange curve) is examined in each subplot.

## Discussion

Here, as a further step, we would like to show that the guided-mode can be efficiently controlled and converted by designing waveguides with variable sections. Based on our proposed guide-mode theory (Eqs. (4) and (5)), by changing the width  $l$  in Fig. 6a, such a gradient waveguide is capable of converting the guided-mode pattern from  $N = 3$  to  $N = 1$  smoothly. It is interesting to note that, as shown in Fig. 6b, the waveform in the part of  $N = 1$  is quite regular with a wavelength  $\lambda$  and has an almost constant amplitude. This is a direct evidence that the waveguide can rectify distorted incident waves by reducing the width to permit the single-mode  $N = 1$ . It has been a generally acknowledged fact that a single guided-mode can realize more robust and lower-loss energy propagation than multiple-modes, especially during a long-distance communication<sup>39,40</sup>. Therefore, it unambiguously presents that our metagrating-based

waveguide possesses powerful rectifying capacity, accurately predictable manipulation and potential tunability for a low-loss, long-distance energy transport.

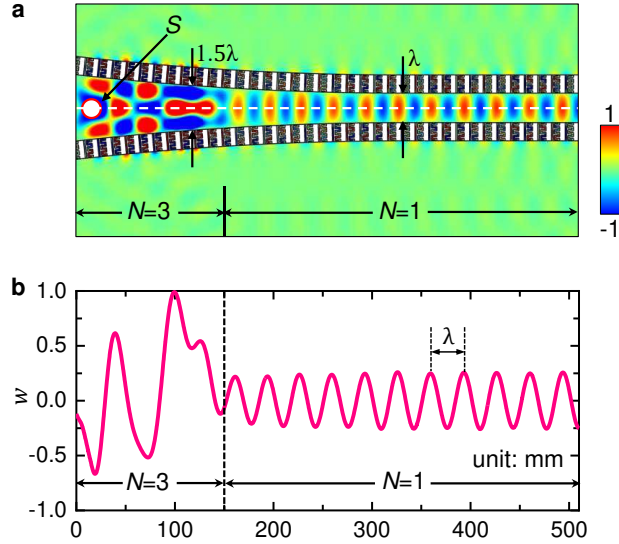


**Figure 6 | Flexural wave pattern excited by a point source in a waveguide with gradient width. (a)** The out-of-plane displacement wave field. **(b)** The out-of-plane displacement  $w$  along the central line of the waveguide (the white dashed line in a).

In conclusion, we present the first realization of an ultrathin waveguide strategy constructed by metagratings. Compared with the topological metamaterials and defected phononic crystals, the most notable paradigm in this work is that the metagrating-based waveguide shows great advantages on ultrathin footprint, broadband performance, and full-angle availability. By designing a bipartite supercell, the proposed metagrating can completely suppress non-zero diffraction orders and transmitted waves. Highly confined omnidirectional-wave-trapping and routing devices are experimentally realized by the proposed waveguide prototype. A modified guided-mode theory is further presented and verified to predict the diffracted guided-mode patterns in waveguides with different values of  $l/\lambda$ . Robust guided-mode tailoring and rectification capability, such as from distorted multiple-mode pattern to uniform single-mode transport, is unambiguously performed. The proposed ultrathin metagrating-based waveguide

opens a new prototype for designing compact, low-loss transport devices for mechanical energy, which may also stimulate analogous research in electromagnetics, acoustics, and other wave physics.

## Methods

**Numerical simulations.** We use COMSOL Multiphysics to conduct a series of full-wave simulations throughout the paper. A thin steel plate with a same height of 1.5mm is investigated as the surrounding medium and the metagratings have the same material parameters with steel plate: Young's modulus  $E = 200$  GPa, density  $\rho = 7930$  kg/m<sup>3</sup> and Poisson's ratio  $\nu = 0.3$ . In all simulations, we apply Perfect Matched Layers (PML) in peripheral boundaries of thin plate to eliminate the effect of reflection. In the simulations of unit cells to obtain phase shift and transmitted amplitude, periodic boundary condition is applied at the top and bottom boundaries.

**Experimental setup.** The actual waveguide sample is a thin steel plate with dimension of  $800 \times 800 \times 1.5$  mm<sup>3</sup>, which is fabricated by wire electrical discharge machining. A 3-cycle tune burst is generated by RIGOL DG4062 signal generator, which is denoted as  $F(t) = [1 - \cos(\frac{2\pi f_c t}{3})] \cdot \sin(2\pi f_c t)$  with a central frequency  $f_c = 15$ kHz. Through the power amplifier (ATA-2022H) the signal is magnified and then transfers to PZT which is bonded on the entrance of waveguide. A Polytec NLV-2500 Laser vibrometer is used to capture the out-of-plane velocity fields by laser beam point by point. The scanning head is fixed on the two-axis motorized translation stage and its moving step  $\Delta d = 4$ mm, which means the spatial resolution is about 8 points per flexural wavelength at 15 kHz. The time-domain response of every point is stored into computer. The sampling rate is set as 1.19 M/s. To improve signal-to-noise ratio, every scanning point is measured 20 times and averaged. In all surrounding boundaries of plate, we use viscoelastic damping material (Blu-Tack) to minimize the effect of reflection. For the sake of comparison with simulation, normalized out-of-plane displacement fields ( $300 \times 240$  mm<sup>2</sup> in the region of waveguide) at different frequencies are obtained through fast Fourier transform based on the acquired data in experiment.

## References

1. Ramo, S., Whinnery, J. R. & Duzer, T. V. *Fields and Waves in Communications Electronics* (John Wiley and Sons, 1984).
2. Sarasin, E. Jean Daniel Colladon. *Nature* **48**, 396-397 (1893).
3. Hecht, J. *City of light: the story of fiber optics* (Oxford University Press, 2004).
4. Knight, J. C., Broeng, J., Birks, T. A. & Russel, P. S. J. Photonic Band Gap Guidance in Optical Fibers. *Science* **282**, 1476-1478 (1998).
5. Okamoto, K. *Fundamentals of optical waveguides* (Academic press, 2006).
6. Ferrera, M. et al. Low-power continuous-wave nonlinear optics in doped silica glass integrated waveguide structures. *Nat. Photonics* **2**, 737-740 (2008).
7. Vahala, K. J. Optical microcavities. *Nature* **424**, 839-846 (2003).
8. Kinsler, L., Frey, A. R., Coppens, A. B., & Sanders, J. V. *Fundamentals of acoustics* (John Wiley & Sons, 1999).
9. Torres, M., de Espinosa, F. R. M., Garcia-Pablos, D. & Garcia, N. Sonic band gaps in finite elastic media: Surface states and localization phenomena in linear and point defects. *Phys. Rev. Lett.* **82**, 3054-3057 (1999).
10. Wu, T. C., Wu, T. T., & Hsu, J. C. Waveguiding and frequency selection of Lamb waves in a plate with a periodic stubbed surface. *Phys. Rev. B.* **79**, 104306 (2009).
11. Kafesaki, M., Sigalas, MM. & Garcia, N. Frequency modulation in the transmittivity of wave guides in elastic-wave band-gap materials. *Phys. Rev. Lett.* **85**, 4044 (2000).
12. Wang, P., Lu, L., & Bertoldi, K. Topological phononic crystals with one-way elastic edge waves. *Phys. Rev. Lett.* **115**, 104302 (2015).
13. Mousavi, S. H., Khanikaev, A. B. & Wang, Z. Topologically protected elastic waves in phononic metamaterials. *Nat. Commun.* **6**, 8682 (2015).
14. He, C. et al. Acoustic topological insulator and robust one-way sound transport. *Nat. Phys.* **12**, 1124-1129 (2016).
15. Lu, J. Y., Qiu, C. Y., Ye, L. P., Fan, X. Y., Ke, M. Z., Zhang, F. & Liu, Z. Y. Observation of topological valley transport of sound in sonic crystals. *Nat. Phys.* **13**, 369-374 (2017).
16. Zhang, Z. W., Wei, Q., Cheng, Y., Zhang, T., Wu, D. J. & Liu, X. J. Topological creation of acoustic pseudospin multipoles in a flow-free symmetry-broken metamaterial lattice. *Phys. Rev. Lett.* **118**, 084303 (2017).
17. Peng, Y. G. et al. Experimental demonstration of anomalous Floquet topological insulator for sound. *Nat. Commun.* **7**, 13368 (2016).
18. Li, F., Huang, X. Q., Lu, J. Y., Ma, J. H. & Liu, Z. Y. Weyl points and Fermi arcs in a chiral phononic crystal. *Nat. Phys.* **14**, 30-34 (2018).
19. Ma, G. C., Xiao, M. & Chan, C. T. Topological phases in acoustic and mechanical systems. *Nat. Rev. Phys.* **1**, 281-294 (2019).
20. Yu, N. et al. Light propagation with phase discontinuities: generalized laws of reflection and refraction. *Science* **334**, 333-337 (2011).
21. Kildishev, A. V., Boltasseva, A. & Shalaev, V. M. Planar Photonics with Metasurfaces. *Science* **339**, 1232009 (2013).

22. Assouar, B., Liang, B., Wu, Y., Li, Y., Cheng, J. C. & Jing, Y. Acoustic metasurfaces. *Nat. Rev. Mater.* **3**, 460-472 (2018).
23. He, Q., Sun, S. L., Xiao, S. Y., & Zhou, L. High-efficiency metasurfaces: principles, realizations, and applications. *Adv. Opt. Mater.* **6**, 1800415 (2018).
24. Cai, X. B., Huang, Z. D. & Yang, J. Traveling Sound Wave with Transverse Particle Velocity in a Metawaveguide by Using a Phase-Reversible Metasurface. *Phys. Rev. Appl.* **14**, 054025 (2020).
25. Xie, Y. B., Wang, W. Q., Chen, H. Y., Konneker, A., Popa, B. I. & Cummer, S. A. Wavefront modulation and subwavelength diffractive acoustics with an acoustic metasurface. *Nat. Commun.* **5**, 5553 (2014).
26. Sun, S. L., He, Q., Xiao, S. Y., Xu, Q., Li, X., & Zhou, L. Gradient-index meta-surfaces as a bridge linking propagating waves and surface waves. *Nat. Mater.* **11**, 426-431 (2012).
27. Zhu, H. F. & Semperlotti, F. Anomalous refraction of acoustic guided waves in solids with geometrically tapered metasurfaces. *Phys. Rev. Lett.* **117**, 034302 (2016).
28. Liu, Y. Q., Liang, Z. X., Liu, F., Diba, O., Lamb, A. & Li, J. S. Source illusion devices for flexural Lamb waves using elastic metasurfaces. *Phys. Rev. Lett.* **119**, 034301 (2017).
29. Wakatsuchi, H., Kim, S., Rushton, J. J. & Sievenpiper, D. F. Waveform-Dependent Absorbing Metasurfaces. *Phys. Rev. Lett.* **111**, 245501 (2013).
30. Cao, L. Y. et al. Flexural wave absorption by lossy gradient elastic metasurface. *J. Mech. Phys. Solids* **143**, 104052 (2020).
31. Kim, M. S., Lee, W., Park, C. I. & Oh, J. H. Elastic wave energy entrapment for reflectionless metasurface. *Phys. Rev. Appl.* **13**, 054036 (2020).
32. Wong, W. C., Wang, W., Yau, W. T. & Fung, K. H. Topological theory for perfect metasurface isolators. *Phys. Rev. B* **101**, 121405 (2020).
33. Zhu, H. F., Walsh, T. F. & Semperlotti, F. Total-internal-reflection elastic metasurfaces: Design and application to structural vibration isolation. *Appl. Phys. Lett.* **113**, 221903 (2018).
34. Ra'di, Y., Sounas, D. L. & Alu, A. Metagratings: Beyond the Limits of Graded Metasurfaces for Wave Front Control. *Phys. Rev. Lett.* **119**, 067404 (2017).
35. Paniagua-Dominguez, R. et al. A Metalens with a Near-Unity Numerical Aperture. *Nano Lett.* **18**, 2124 (2018).
36. Fu, Y. Y. et al. Reversal of transmission and reflection based on acoustic metagratings with integer parity design. *Nat. Commun.* **10**, 2326 (2019).
37. Li, B., Hu, Y. B., Chen, J. L., Su, G. Y., Liu, Y. Q., Zhao, M. Y. & Li, Z. Efficient asymmetric transmission of elastic waves in thin plates with lossless metasurfaces. *Phys. Rev. Appl.* **14**, 054029 (2020).
38. Zhu, H. F., Walsh, T. F. & Semperlotti, F. Experimental study of vibration isolation in thin-walled structural assemblies with embedded total-internal-reflection metasurfaces. *J. Sound Vib.* **456**, 162-172 (2019).
39. Patel, R. N., Wang, Z. Y., Jiang, W. T., Sarabalis, C. J., Hill, J. T. & Safavi-Naeini, A. H. Single-mode phononic wire. *Phys. Rev. Lett.* **121**, 040501 (2018).
40. Romero, E., Kalra, R., Mauranyapin, N. P., Baker, C. G., Meng, C. & Bowen, W. P. Propagation and Imaging of Mechanical Waves in a Highly Stressed Single-Mode Acoustic Waveguide. *Phys. Rev. Appl.* **11**, 064035 (2019).

## **Acknowledgements**

This work is supported by the National Natural Science Foundation of China (NSFC) under G Grant No. 11902262, No. 11902239.

## **Author contributions**

B.L., Y.L. and Y.H. conceived the original idea. Y.H., Y.Z., Y.L. and B.L. performed the theoretical calculation and numerical simulation. Y.H., Y.Z. and G.S. carried out the experiments and analyzed the data. Z.L. and M.Z. helped with the theoretical interpretation. Y.H., B.L. and Y.L. wrote the manuscript. Y.L. and B.L. supervised the project. All authors contributed to scientific discussions and modifications of the manuscript.

## **Additional information**

**Supplementary Information** accompanies this paper at [URL will be inserted by publisher] for [Supplementary Figures 1-6](#), [Supplementary Notes 1-5](#) and [Supplementary Movies 1-6](#).

**Competing interests:** The authors declare no competing interests.

## Supplementary Files

This is a list of supplementary files associated with this preprint. Click to download.

- [supplementarymaterialcommunicationsphysics.docx](#)
- [Movie1.gif](#)
- [Movie2.gif](#)
- [Movie3.gif](#)
- [Movie4.gif](#)
- [Movie5.gif](#)
- [Movie6.gif](#)